Progress of Theoretical Physics, Vol. 78, No. 6, December 1987

Fragmentation of Isothermal Sheet-Like Clouds. II

—— *Full Nonlinear Numerical Simulations* ——

Shoken M. MIYAMA, Shinji NARITA* and Chushiro HAYASHI**,*)

Department of Physics, Kyoto University, Kyoto 606
**Department of Electronics, Dōshisha University, Kyoto 602*
***Momoyama Yogoro-cho 1, Fushimi-ku, Kyoto 612*

(Received August 24, 1987)

The fragmentational instability of an infinite isothermal gas layer, extending infinitely in the x- and y-direction, is investigated by means of three-dimensional numerical simulations. The nonlinear growth of perturbations with the initial wave pattern, $\cos(k_x x)\times\cos(k_y y)$, is calculated for various values of the wave numbers k_x and k_y. For unstable modes, the fragmentation of a layer and the subsequent collapse of fragments are simulated. It is found that, if the ratio, k_y/k_x, is in the range, 0.8−1.2, each fragment collapses almost axisymmetrically without flattening along the z-axis. However, if the ratio is greater than 1.2 or less than 0.8, each fragment becomes more and more slender as it collapses and finally a thin filament is formed. We also calculate the growth of random perturbations and confirm that a large number of filaments are formed.

As a result of the computations, we construct a scenario of fragmentation and subsequent evolution of a sheet-like cloud such that most of the fragments become finally thin filaments and re-fragment. This scenario explains why filamentary structures often appear in interstellar clouds observed. We also find that the mass function of the final fragments is expressed in the form, $N \propto m^{-2}$, where N and m are the number and mass, respectively.

§ 1. Introduction

This is the second paper in a series studying the nonlinear effect on the growth of perturbations in the sheet-like clouds. In Paper I,[1] we described the motivation of this study, reviewed the linear perturbation theory and obtained solutions of the second-order perturbation equations. These solutions show that the second-order effect enlarges the axis ratio of the collapsing fragments.

In this paper, we compute the fragmentation processes of an isothermal sheet by three-dimensional numerical simulation, in order to analyze the fully-nonlinear effect on the growth of perturbations. Using the results of these computations we aim at clarifying the following points. (1) How does an isothermal sheet fragment and why does such a filamentary structure appear often in nature? (2) What structure does each fragment have? Numerical data obtained may also be useful to know the initial condition for star formation. (3) What is the mass distribution of the fragments? This relates to the initial mass function of stars. (4) Because we know the solution of the linearized perturbation equation, we can make a critical test of our three-dimensional computations themselves by comparing our numerical solutions in stages of small amplitudes with the linear solutions.

In this paper, we make the same simplifications and assumptions as in Paper I. (1) The equation of state is assumed to be isothermal. (2) The sheet-like cloud extends to infinities in the x- and y-direction. We assume periodic boundary condi-

*) Emeritas Professor of Kyoto University.

tions in these directions. In the remaining z-direction, the cloud has a finite size because we assume the presence of small but finite external pressure. We use the periodic boundary condition not only for the mathematical reason but also for the purpose to find the gravitational effect of neighboring condensations on the formation and the collapse of each condensation.

The unperturbed state of a sheet-like cloud is a self-gravitating equilibrium gas layer which has a vertical density distribution (see Paper I)

$$\rho_0(z)=\rho_{00}\mathrm{sech}^2(z/z_0) \qquad \text{for } |z|\leqq z_b\,, \tag{1·1}$$

where ρ_{00} is the unperturbed density at $z=0$, (i.e., $\rho_{00}=\rho_0(0)$). The scale height z_0 is defined by using the constant sound velocity c_s as

$$z_0=c_s/(2\pi G\rho_{00})^{1/2} \tag{1·2}$$

and $|z|=z_b$ denotes the boundary of the layer where the gas pressure is equal to the external pressure, P_{ext} $(=c_s{}^2\rho(z_b))$. Initially, this equilibrium layer has small-amplitude perturbations and we calculate their growth toward the stage of nonlinear amplification.

In § 2, the method of computation is shown briefly and in § 3 the results of numerical simulations are given. Discussion on the scenario of fragmentation of clouds and on the mass function of fragments together with conclusions is given in § 4. In the Appendix, we describe our computational method of calculating gravitational force in the case of a periodic boundary condition.

§ 2. Method of numerical computations

2.1. *Three-dimensional hydrodynamical code*

The numerical method used in this work is one of the Lagrangian methods which is so-called the smoothed particle method developed by Miyama, Narita and Hayashi.[2] In this method, a cloud is divided into a number of fluid elements which are called particles. Each particle has the same mass and its own internal density distribution. Local densities of the fluid are given by the superposition of density distributions of all the particles.

The motion of fluid is represented by a set of motion of all the particles. The equation of motion of each particle is

$$d\boldsymbol{v}_i/dt=-(\nabla P/\rho)_i+\boldsymbol{F}_i+\boldsymbol{S}_i\,, \tag{2·1}$$

where $\boldsymbol{v}_i$, $\boldsymbol{F}_i$ and $\boldsymbol{S}_i$ are velocity, gravitational force and artificial viscosity force at the center of mass of the i-th particle, respectively. Because we assume an isothermal gas, the pressure gradient term is calculated from the density gradient. In this paper all the physical quantities are assumed to be periodic in the x- and y-direction. Therefore, differently from our previous work,[2] we obtain the gravitational force by solving the Poisson equation, using a finite difference method described in the Appendix. The viscosity force S_i is used to reproduce plane shock phenomena numerically. Detailed formula for S_i will be described elsewhere.[3]

2.2. *Boundary conditions*

In the x- and y-direction, we assume periodic boundary conditions. In terms of the lattice constants, x_L and y_L, we define new variables, X and Y, as

$$X=x/x_L+y/y_L \quad \text{and} \quad Y=x/x_L-y/y_L \tag{2·2}$$

and we assume that any physical quantity, f, satisfies the condition

$$f(X\pm1, Y\pm1)=f(X, Y) \text{ where } -1/2<X, Y\leqq 1/2\,. \tag{2·3}$$

At the boundary in the z-direction, the pressure is always equal to P_{ext}, and this is called the pressure-constant boundary condition (PCBC). In our smoothed particle method, it is very difficult to set exact PCBC. So we adopt an approximate procedure such that, for the particle whose density is less than the boundary density $\rho_b(=P_{\text{ext}}/c_s^2)$, the pressure gradient is modified as

$$(\boldsymbol{\nabla} P/\rho)_i \longrightarrow (\boldsymbol{\nabla} P/\rho)_i(\rho_i/\rho_b)\times\max(\rho_i/\rho_b-0.8, 0) \text{ if } \rho_i<\rho_b\,. \tag{2·4}$$

The above formula and the numerical value 0.8 have been determined after many test computations. We have found that in the case of Eq. (2·4) the minimum density of all the particles remains to be almost ρ_b. This shows that Eq. (2·4) gives a very simple and powerful approximation to PCBC.

In this paper, the ratio $\rho_0(0)/\rho_b$ for all the simulations is fixed to 8. In the linear perturbation theory, the dispersion relation for $\rho_0(0)/\rho_b=8$, is very close to that for $\rho_0(0)/\rho_b=\infty$ (see Fig. 1 in Paper I). Namely, the growth of perturbation does not depend sensitively on the value of $\rho(0)/\rho_b$ as far as it is much greater than unity.

2.3. *Construction of an initial unperturbed state*

In our simulation, an unperturbed state with the density distribution given by Eq. (1·1) is constructed in the following way. We impose the external gravitational force,

$$\boldsymbol{F}=-(2c_s^2/z_0)\tanh(z/z_0)(\boldsymbol{z}/|z|)\,, \tag{2·5}$$

and also the strong damping term $-\boldsymbol{v}/\tau$, where τ is a constant. Then we integrate the particle's equation of motion,

$$d\boldsymbol{v}_i/dt=-(\boldsymbol{\nabla} P/\rho)_i+\boldsymbol{F}(z_i)-\boldsymbol{v}_i/\tau\,, \tag{2·6}$$

until velocities of all the particles become small enough. Finally we obtained a density distribution which is in agreement with Eq. (2·1) within a 2% error. From this distribution, we compute gravitational force using a method described in the Appendix. Comparing this force with Eq. (2·5), we found that the error is less than 3%.

In our computations, we use 5000 particles with $64\times64\times32$ meshes for gravity calculation in the case $k_x=k_y$ and 8333 particles with $144\times48\times32$ meshes in the case $k_y/k_x=3$ (for k_x and k_y see Eq. (3·1)).

§ 3. Numerical simulations of growth of perturbations

Because the solutions of the linear perturbation equation form a complete set, any small perturbation in the sheet-like clouds can be expanded using these eigenfunctions. Therefore first investigate how each of the eigenmodes grows nonlinearly. After that we simulate the growth of random perturbations, in order to obtain a whole view of fragmentation of the clouds.

3.1. *Initial condition for the case of a pure eigenmode*

We take the equilibrium isothermal sheet (Eq. (1·1)) with a small perturbation as the initial condition of numerical simulations. For the initial perturbation, we adopt the eigenmode solutions of the perturbation equation as shown in Paper I. As to the numerical treatment of constructing the initial condition, the velocity perturbation is simpler than the density perturbation. Therefore, for simplicity, we choose a mode of the velocity perturbation which is written as

$$\left.\begin{aligned} &\rho_1/\rho_0 = f(z)\cos(k_x x)\cos(k_y y)\sinh(\omega t)\,, \\ &\psi_1/{c_s}^2 = g(z)\cos(k_x x)\cos(k_y y)\sinh(\omega t)\,, \\ &\boldsymbol{v}_1/c_s = -c_s/\omega\cdot\nabla\{(f+g)\cos(k_x x)\cos(k_y y)\}\cosh(\omega t)\,, \end{aligned}\right\} \tag{3·1}$$

where $f(z)$ and $g(z)$ are the eigenfunctions in the linear theory. Then the initial data for simulation are written as

$$\left.\begin{aligned} &\rho_1/\rho_0 = 0\,, \\ &\psi_1/{c_s}^2 = 0\,, \\ &\boldsymbol{v}_1/c_s = -c_s/\omega\cdot\nabla\{(f+g)\cos(k_x x)\cos(k_y y)\}\,. \end{aligned}\right\} \tag{3·2}$$

Because of the spatial periodicity assumed, we have only to consider the region where

$$\left.\begin{aligned} &-\pi/2 < k_x x + k_y y \leqq \pi/2\,, \\ &-\pi/2 < k_x x - k_y y \leqq \pi/2\,. \end{aligned}\right\} \tag{3·3}$$

We can characterize the initial data by the following 4 parameters.

(1) $\rho_0(0)/\rho_b$: the ratio of the central density to the boundary density in an unperturbed state. This parameter represents the property of cloud's circumstance. As mentioned above, this factor is fixed to 8 in this paper.

(2) ε: the initial magnitude of perturbation (e.g., $\rho=\rho_0+\varepsilon\rho_1+\varepsilon^2\rho_2+\cdots$). In this paper, the value of ε is fixed to 0.1. For this value of ε, the nonlinear effect at the initial stage is negligibly small. If we choose a smaller value of ε, we need only a longer time of computation.

(3) kz_0: the normalized wave number of where $k^2={k_x}^2+{k_y}^2$. The growth time in the linear theory depends only on the value of kz_0.

(4) k_y/k_x: the ratio of wave numbers which represents the initial shape of perturbation in the (x, y) plane.

We fix the values of $\rho_0(0)/\rho_b$ and ε and compute the growth of perturbation for various values of kz_0 and k_y/k_x. For the units of time, we adopt the free fall time at

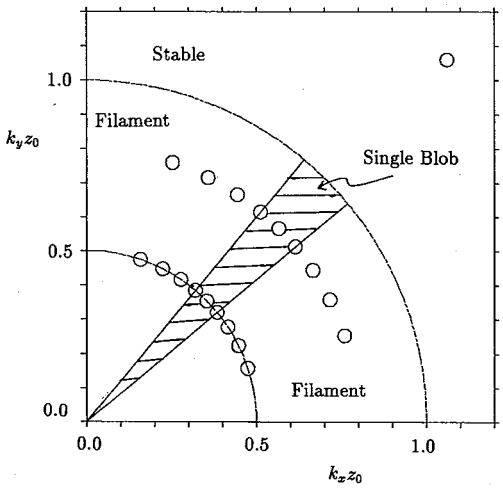

Fig. 1. The data of the initial perturbation in the wave-number space (k_x, k_y). The values of ($k_x z_0$, $k_y z_0$) adopted in the numerical computations are shown by the circles. The curves, $kz_0=1$ and $kz_0=0.5$, are shown by the dashed curves. According to the linear perturbation theory, the perturbations with $kz_0>1$ are stable and those with $kz_0\sim 0.5$ are most unstable. The results of nonlinear simulations show that, if the wave numbers of the initial perturbation lie in the hatched region, the cloud fragments and each fragment collapse as a single blob. However, for the wave numbers lying in the other region with $kz_0<1$, the cloud fragments and each fragment collapse to form a very slender filament.

the cloud boundary, i.e., $(3\pi/32G\rho_b)^{1/2}$.

The values of k_x and k_y adopted in the numerical computations are shown by the circles in Fig. 1. We compute the three cases for kz_0, i.e., $kz_0=0.5, 0.8$ (both are unstable modes) and $kz_0=1.5$ (a stable mode). For each of the cases, $kz_0=0.5$ and 0.8, we compute 5 cases where $k_y/k_x=1$, 1.2, 1.5, 2 and 3. In the case $kz_0=1.5$, we compute only one case, $k_x=k_y$. In the following, first we show the result of the stable mode ($kz_0=1.5$), which is also useful as a test of our numerical method. Next we show the results of the two unstable cases ($kz_0=0.5$, $k_y/k_x=1$) and ($kz_0=0.5$, $k_y/k_x=2$),which are typical examples indicating strong dependence on the ratio k_y/k_x.

3.2. *A result of a stable mode* ($kz_0=1.5$, $k_x=k_y$)

This mode is stable according to the linear analysis. Therefore the main aim of the computation of this mode is to test the ability of our numerical method. In order to express the growth of perturbation most simply, we consider $\delta\rho/\rho_0$ at the origin of the coordinates, i.e.,

$$\delta\rho/\rho_{00}=\rho(\boldsymbol{x}=0)/\rho_{00}-1\,. \tag{3·4}$$

In Fig. 2, we show the time variation of $\delta\rho/\rho_{00}$ and also show the behavior of the linear solution for comparison. Because the initial amplitude is very small, the agreement is very good, as it should be, except for small noisy oscillations arising from the noises which remain undamped in the construction of the unperturbed state (see § 2.3). Figure 2 shows that the numerical computational method used here is reliable. Also from the fact that the amplitude of the oscillation is almost constant, it is seen that the artificial viscosity term, which has been introduced to simulate a shock process, does not give a bad influence upon the numerical results.

3.3. *Typical results for unstable modes*

a) a mode with $kz_0=0.5$ and $k_x=k_y$ (model A)

The eigenmode with $kz_0=0.5$ is the almost fastest growing mode. The variations of $\delta\rho/\rho_{00}$ with time are shown in Fig. 3, where the curves by $\delta\rho/\rho_{00}$ and $\varepsilon\rho_1/\rho_{00}$ represent the numerical results and the linear solution for $\varepsilon=0.1$, respectively. Because only the velocity perturbations are given initially, we have $\delta\rho/\rho=0$ at $t=0$. It is clearly seen that, for $\delta\rho/\rho<0.2$, our numerical result is in close agreement with

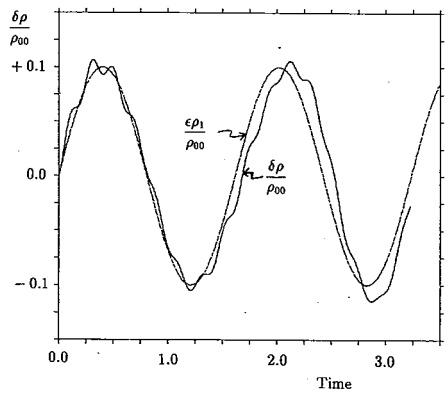

Fig. 2. The time variation of $\delta\rho/\rho_{00}$ for the stable mode with $kz_0=1.5$ and $k_x=k_y$. The solution of the linear equation is also shown by the dashed curve, $\varepsilon\rho_1/\rho_{00}$.

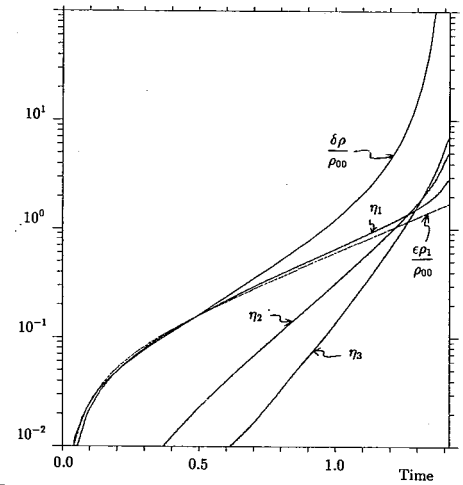

Fig. 3. The growth of the density perturbation in the case, $kz_0=0.5$ and $k_x=k_y$ (model A). The time variation of $\delta\rho/\rho_{00}$ at $x=y=z=0$ is shown by the solid curve. The time variation given by the linear perturbation theory is shown by the dotted curve: $\varepsilon\rho_1/\rho_{00}$. The amplitudes of the Fourier components of the density at $z=0$, η_1, η_2 and η_3 are also plotted.

the linear solution. Our numerical code passes a test also in the case of an unstable mode.

In order to analyze the behavior of nonlinear growth of perturbations, let us consider the Fourier components of density. The density at $z=0$ is decomposed into the Fourier series as

$$\rho(z=0)=\sum_{m,n}\hat{\rho}_{m,n}e^{i(mk_xx+nk_yy)}. \tag{3·5}$$

Now, we define

$$\eta_{m,n}\equiv\hat{\rho}_{m,n}/\hat{\rho}_{0,0}(t=0), \tag{3·6}$$

$$\eta_1=\sum_{n=\pm1}(\eta_{1,n}+\eta_{-1,n}), \tag{3·7}$$

$$\eta_2=\sum_{n=0,\pm2}(\eta_{2,n}+\eta_{0,n}+\eta_{-2,n})-1, \tag{3·8}$$

$$\eta_3=\sum_{n=\pm1,\pm3}(\eta_{3,n}+\eta_{1,n}+\eta_{-1,n}+\eta_{-3,n}). \tag{3·9}$$

Here, η_1 represents the amplitude of the normal mode, and η_2 and η_3 represent the amplitudes of the second and third harmonics, respectively. These components are also shown in Fig. 3. The time variation of η_1 is very close to that of the linear solution until $\delta\rho/\rho_{00}$ grows to 1. This result shows that the nonlinear wave-wave interaction works mainly in the direction to generate higher wave-number waves and does not work well in the generation of lower wave-number ones.

As shown in Paper I, the amplitude of the second harmonics η_2 must grow as $\exp(2\omega t)$, when t is large enough. This behavior is also seen in Fig. 3.

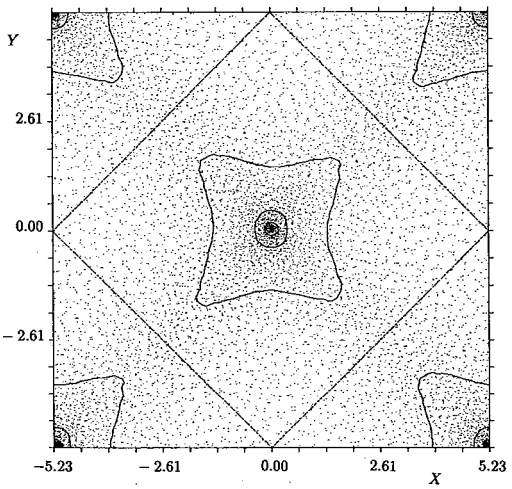

Fig. 4. The particle positions projected onto the $z=0$ plane and the density contours in the same plane for model A at time $t=1.4$. The broken lines denote the periodic boundaries.

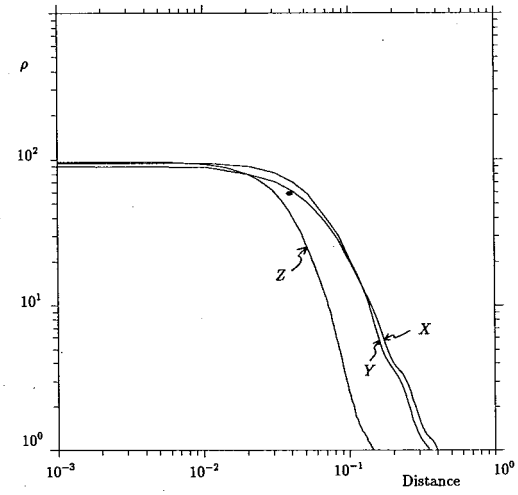

Fig. 5. The density structure of the cental blob shown in Fig. 4. The density distributions along the x-, y- and z-axis are shown. In the envelope densities along the x- and y-axis decrease as R^{-2}.

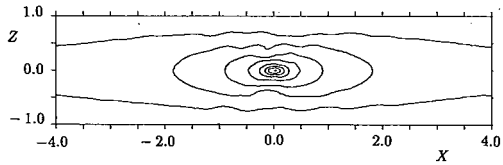

Fig. 6. The density contours in the $y=0$ plane for model A at time $t=1.4$.

In Fig. 4, we show all the position of particles projected onto the plane, $z=0$, and also show the density contours in the same plane. The broken lines denote the periodic boundaries. The density contours near the center are almost axisymmetric. In order to see the density structure of this axisymmetric region, the density distributions along the x-, y- and z-axis are shown in Fig. 5. The densities along the x- and y-axis are almost constant near the center and decrease as $R^{-2}(=(x^2+y^2)^{-1})$ in the outer region. It is to be noted that this type of density distribution appears often in the inner region of an isothermal axisymmetric collapsing cloud.[4)~6)] In Fig. 6, we show the density contours in the $y=0$ plane. The shape of the central region in the (x, z) plane is not spherical but slightly flattened and the axis ratio is almost equal to 2. The central, where the density is high enough, has a very compact size compared with the distance between two neighboring condensations. This means that the central region collapses as a nearly isolated system since the gravitational effect of neighboring condensation is very small.

Will this isolated blob fragment into many pieces? The flatness of a cloud determines whether a cloud will fragment or not. Here we define the flatness of a cloud by the ratio a_x/a_z where a_x and a_z are the lengths of the x- and z-axis, respectively, of an equi-density surface. The time variations of the flatness of equi-density surfaces with $\rho/\rho_{\max}=1/2, 1/\sqrt{10}$ and $1/10$ are shown in Fig. 7, where $\rho_{\max}$ is the maximum density at a time considered. For all the values of $\rho/\rho_{\max}$, the flatness decreases to about 2 as the perturbation grows (see also Fig. 6). Hence the possibility

that the cloud will re-fragment is small because the flatness a_x/a_z must be greater than π (i.e., $kz_0<1$) for the fragmentation to occur (see, e.g., Fig. 1 in Paper I).

In the case where $kz_0=0.8$ and $k_x=k_y$, the behavior of perturbation growth is very similar to the above case ($kz_0=0.5$ and $k_x=k_y$), except for a longer time of growth.

b) a mode with $kz_0=0.5$ and $k_y/k_x=2$ (model B)

Figure 8 shows the growth of the total perturbation as well as its components, η_1 and η_2. Furthermore, the time variations of η_{02} and η_{20}, which are the amplitudes of the waves $\cos(2k_yy)$ and $\cos(2k_xx)$, respectively, are also shown. It is clearly seen that we have $\eta_{02}>\eta_{20}$, in agreement with the analytic result obtained in Paper I. Namely if initially the perturbation has a longer wavelength along the x-axis than that along the y-axis, e.g., $\lambda_x/\lambda_y=2$, the amplitude of $\cos(2k_yy)$ grows more rapidly than that of $\cos(2k_xx)$ and the axis ratio λ_x/λ_y becomes larger than 2 (see Fig. 3 in Paper I). This is more clearly seen in Fig. 9, where the projected particle positions at $t=1.19$ (Fig. 9(a)) and $t=1.40$ (Fig. 9(b)) are shown. The axis ratio of dense regions is clearly increased with time.

Figure 10 shows the time variations of the axis ratios, a_x/a_y and a_y/a_z, of the equi-density contours with various values of $f=\rho/\rho_{\max}$. After the nonlinear effect becomes large ($t\geqq1.2$, see also Fig. 8), the ratio a_x/a_y grows rapidly. On the other hand, the ratio a_y/a_z decreases only with time and finally becomes unity. That is, the collapsing object becomes a slender cylinder. In Appendix B of Paper I, we showed a similarity solution for the isothermal collapse of an infinite cylinder. According to this solution, the collapsing cylinder contains an inner region, where the density is almost constant, and an envelope, where the density drops as R^{-4} (R being the distance from the axis). In Fig. 11, we show the density distribution found by our

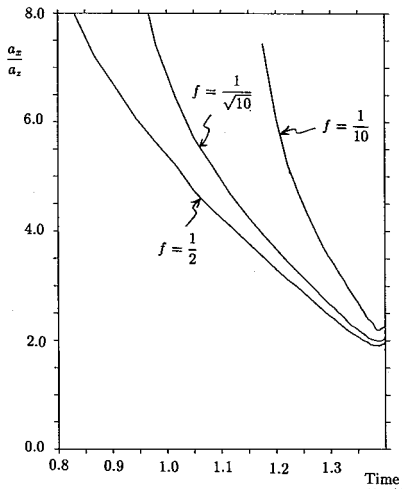

Fig. 7. The time variations of the flatness of equi-density surfaces in model A. We choose the equi-density surfaces such that the ratio $f\equiv\rho/\rho_{\max}$, where ρ is the surface density and $\rho_{\max}$ is the maximum density in the cloud, takes the constant values. The flatness is defined as the ratio, a_x/a_z, where a_x and a_z are the length of the x- and z-axis, respectively.

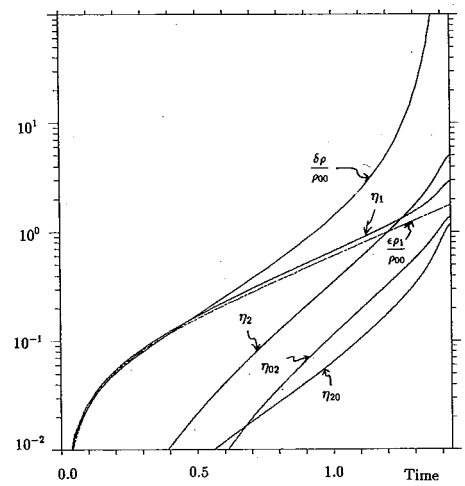

Fig. 8. The same as shown in Fig. 3 for the case, $kz_0=0.5$ and $k_y=2\times k_x$ (model B). The amplitude of the Fourier components of the density at $z=0$, η_1, η_2 and the second-order components η_{02} and η_{20} are also plotted.

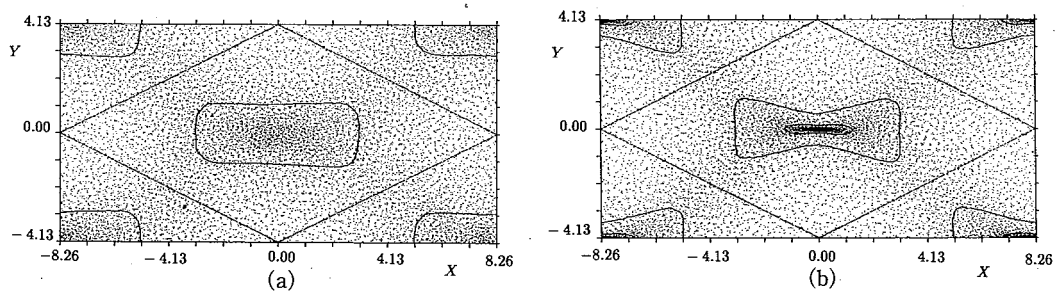

Fig. 9. The particle positions projected onto the plane of $z=0$ and the density contours at the same plane for model B, (a) at $t=1.19$ and (b) at $t=1.40$. The broken lines denote the periodic boundaries.

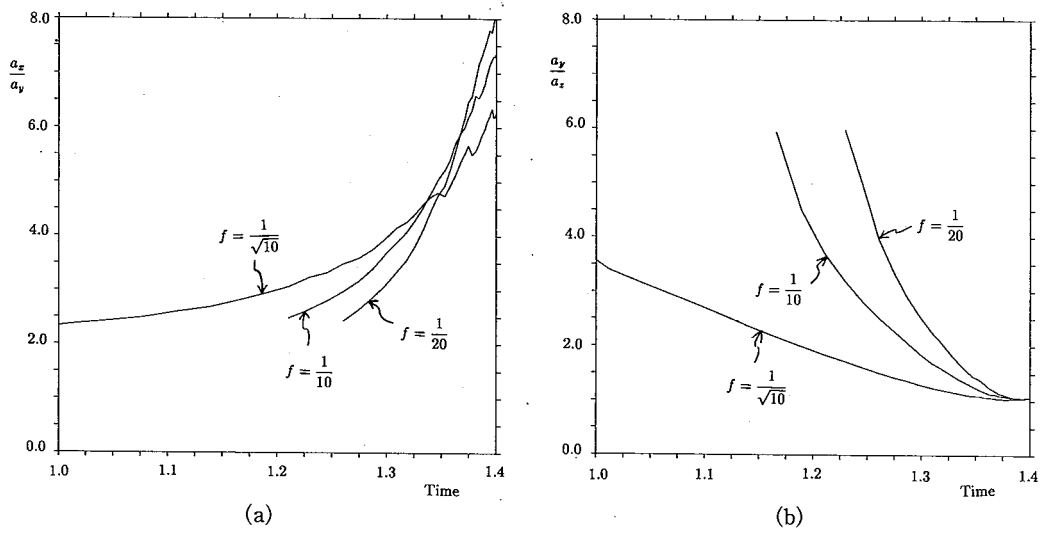

Fig. 10. The time variations of the axis ratios, a_x/a_y and a_y/a_z, of the equi-density surfaces in model B. The label f denotes the ratio, ρ/ρ_{max} for the surfaces.

computation, which is at the same stage as shown in Fig. 9(b). The density distributions along the y- and z-axis, which are perpendicular to the cylindrical axis, are nearly proportional to R^{-4}. Therefore the collapse of the filamentary region shown in Fig. 9(b) is essentially the cylindrical collapse.

According to Appendix B of Paper I, the high density region of the cylinder becomes slender and slender, and this collapse may continue until the density becomes so high that the filament becomes opaque to radiation. Then the equation of state changes from an isothermal one to an adiabatic one. Finally the collapse stops and a very thin filament will be formed. The equilibrium cylinder is always unstable to fragmentation along its axis. In conclusion, the fragment of the sheet-like cloud which contains the initial perturbation with $kz_0=0.5$ and $k_y/k_x=2$, collapses to a filament which finally re-fragments into a large number of dense clumps.

The above-mentioned behavior is also seen in the cases of different modes with $k_y/k_x>1.2$ (or $<1/1.2$) and $kz_0=0.5$ as well as 0.8. In the case where $kz_0=0.8$, the growth time of perturbation is slightly longer.

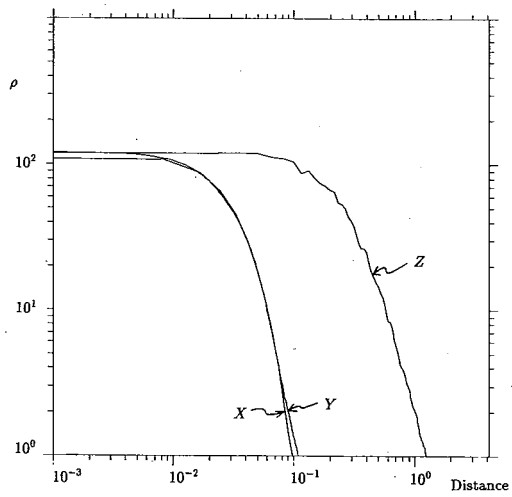

Fig. 11. The density structure of the cental filamentary region shown in Fig. 8(b). The density distributions along the x-, y- and z-axis are shown. The densities along the y- and z-axis decrease as R^{-4} in the envelope. This is a characteristic feature of a cylindrical collapse.

3.4. *Comparison of modes with the same k but different k_y/k_x*

In this subsection, we show how the growth of the perturbations with the same value of k depends on the ratio k_y/k_x.

First let us compare the growth time of perturbation. The time spent until $\delta\rho/\rho_{00}$ grows to 1 and 10 is tabulated in Table I, for the cases where $kz_0=0.5$ and 0.8. The growth time depends mainly on the value of k and does not depend sensitively on the ratio k_y/k_x, in qualitative agreement with the linear perturbation theory.

Next the axis ratio a_x/a_y of an equi-density surface with the density, $\rho=0.1\times\rho_{\max}$, is plotted as a function of $\delta\rho/\rho_{00}$ in Fig. 12 for various models. For a model with $k_y/k_x>1.2$ (or $<1/1.2$), the axis ratio becomes greater than 4 before $\delta\rho/\rho_{00}$ grows to 10^4. This value of the ratio, 4, is a critical (smallest) value for the occurrence of fragmentation of an isothermal infinite cylinder.[1] Accordingly, the perturbations of these modes will grow to form filaments which fragment again after the collapse stops. On the contrary, in the mode with $k_y/k_x\leqq1.2$ (and $\geqq1/1.2$), the axis ratio does not grow large before $\delta\rho/\rho_{00}$ grows to about 10^4.

From the above results, we can construct the following scenario of evolution of the sheet-like clouds. When the sheet is formed, there are many modes of perturbation in the cloud. As shown in Fig. 1, the evolution of perturbation is grouped into three types according to the wave number, i.e., the position in the (k_x, k_y) plane as shown in Fig. 1. One is a stable type ($kz_0>1$). Next is a type which is unstable ($kz_0<1$) and grows to a single high density blob ($1/1.2\leqq k_y/k_x\leqq1.2$). The last is a type

Table I. The growth time of perturbation until $\delta\rho/\rho_{00}$ grows to 1 or 10.

kind of the initial perturbation		growth time[a]	
		$\delta\rho/\rho_{00}=1$	$\delta\rho/\rho_{00}=10$
$kz_0=0.5$	$k_y/k_x=1.0$	0.96	1.28
	$k_y/k_x=1.2$	0.97	1.29
	$k_y/k_x=2.0$	0.94	1.26
	$k_y/k_x=3.0$	0.93	1.25
$kz_0=0.8$	$k_y/k_x=1.0$	1.23	1.62
	$k_y/k_x=1.2$	1.23	1.62
	$k_y/k_x=2.0$	1.24	1.65
	$k_y/k_x=3.0$	1.24	1.69

a) The unit of time is the initial free fall time at the boundary surface where the density is ρ_b.

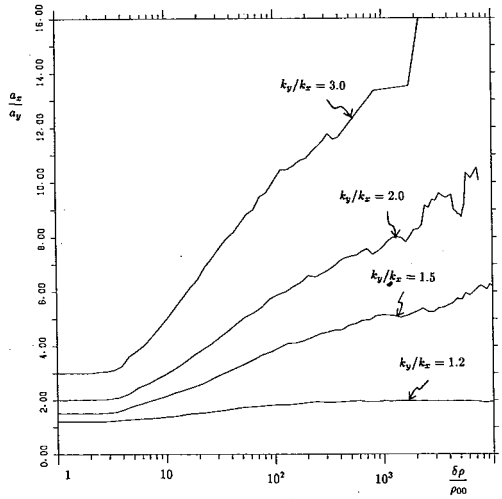

Fig. 12. The axis ratio a_x/a_y of the equi-density surface with $\rho=0.1\rho_{\max}(t)$ versus the value of $\delta\rho/\rho_{00}$ for the perturbations which have the same value of k, $kz_0=0.5$.

which is unstable, grows to a thin filament and re-fragments into many blobs (k_y/k_x >1.2 or $<1/1.2$).

Now, we consider a statistical problem on the spectrum of initial perturbations in the (k_x, k_y) space. Strictly speaking, the spectrum depends on the formation process of the sheet cloud itself, but it is not unreasonable to assume that the spectrum is uniform, at least, in the most unstable region (i.e., a ring-like region around the circle, $kz_0\cong 0.5$) of the (k_x, k_y) space. If this is the case, perturbations with different values of k_y/k_x exist with equal weight along the circle $k=$constant. Then, the probability that the initial ratio k_y/k_x is greater than 1.2 or less than $1/1.2$ is estimated to be about 90%. Namely, 90% of the perturbations in the cloud will grow to thin filaments. In the next subsection we will confirm this by simulation for the case where initial perturbations are completely random.

3.5. *Growth of random velocity fluctuations*

In this subsection, we compute the growth of a perturbation which starts with random velocity fluctuations. The periodic length of the boundary in this case is chosen to be $4\lambda_m$ in both the x- and y-direction, where λ_m is the wavelength of the most unstable mode ($\sim 4\pi z_0$).

As the random velocity fluctuations, we give the following velocity to each particle,

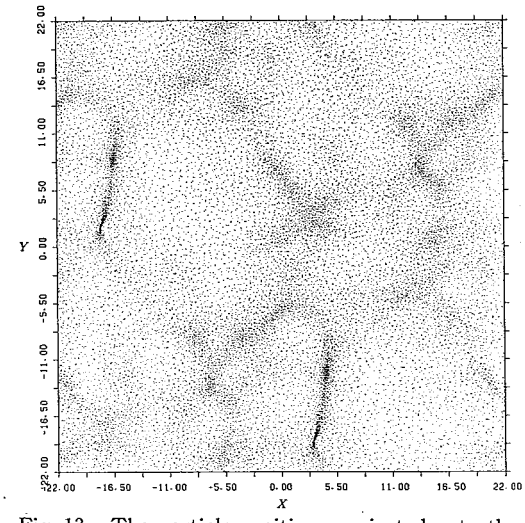

Fig. 13. The particle positions projected onto the plane, $z=0$, for the case of random velocity perturbations.

$$\left.\begin{aligned} v_x &= 0.1 c_s R_m \,, \\ v_y &= 0.1 c_s R_m \,, \\ v_z &= 0 \,, \end{aligned}\right\} \qquad (3\cdot 10)$$

where R_m is a uniform random number in the range $(-1, 1)$.

The result of simulation is shown in Fig. 13. There appear many filamentary structures as expected from the results of the previous subsection. In the case of the random perturbation, most of the values of k_y/k_x is greater than 1.2 or less than $1/1.2$ and, hence, many fluctuations grow to form filamentary structures. But there are a few blob-like condensations, as is also expected. From Fig. 13, the mean

distances between filamentary clouds are found to be about λ_m.

§ 4. Discussion and conclusions

4.1. *Scenario of fragmentation*

Using the results of numerical simulations, we can construct the following scenario of cloud's fragmentation.

(1) A sheet cloud is formed by some triggering mechanism such as a collision between clouds, a compression by supernova explosion, etc.

(2) In the sheet-like cloud formed, there are various types of perturbations with small amplitudes. If we define θ as

$$k_x = k \cdot \cos\theta \text{ and } k_y = k \cdot \sin\theta , \tag{4·1}$$

the number of waves with the same k may be independent of θ.

(3) Perturbations with $kz_0 \leqq 1$ are unstable to fragmentation and those with $kz_0 \cong 0.5$ grow most rapidly.

(4) The axis ratio of a fragment, which starts with the initial ratio $k_y/k_x > 1.2$ or < 1.2, grows greatly as it goes on collapsing. Hence, almost all of the perturbations grow to form filamentary structures. The remaining part (about 10%) of fragments, which have the initial ratio $1.2 \geqq k_y/k_x \geqq 1/1.2$, collapse as single nearly axisymmetric blobs.

(5) Eventually, the density of each fragment becomes so high that the gas is opaque to radiation and the temperature begins to rise. Then the collapse stops.

(6) The cylindrical cloud becomes unstable to fragmentation in the axis direction when its axial length exceeds $\sim 2\pi r_0$, where r_0 is the radius of the cylinder. Then the filament will fragment into many dense clouds. On the contrary, the axisymmetric blob cloud does not fragment.

(6) The rest gas of the original sheet-like cloud accretes onto the final fragments and these fragments begin to collapse again to form proto-stars.

(7) As a result, almost dense clouds have filamentary structures. Within these filaments there are many dense molecular clouds and young stars, which have relatively small masses. Very small parts of clouds collapse as a single object to form a very massive proto-star.

Now we give several comments on the above scenario. The first key point of the above scenario is that a parent cloud, which fragments into many pieces, is a sheet-like cloud. It comes from the fact that the dispersion relation has the maximum growing point at a finite k as shown in Fig. 1 of Paper I. The distances between fragments should be equal to the most unstable wavelength, $\lambda_m = 4\pi z_0$. Actually the observed distances between filamentary molecular clouds in Taurus molecular clouds agree consistently with most unstable wavelength.[7]

The second point is that because of the nonlinear effect almost all the perturbations grow to thin filaments. This explains why molecular clouds often have the filamentary structures.

The third point is the mass of fragments. Larson discussed that this mass is equal to the mass, $\sigma\lambda_m^2$, which comes from the first fragmentation of a sheet, with

column density σ.[8] However we consider that it is rather equal to the mass which comes from the re-fragmentation of a filament and, hence, is much less than $\sigma\lambda_m^2$ (since a filament fragments into many pieces), as will be mentioned in the next subsection.

4.2. *Mass distribution of fragments*

According to the scenario in § 4.1, we can calculate the mass function of fragments. The mass which is contained in a pure eigenmode (k_x, k_y) is

$$M(\theta)=\sigma\lambda_x\lambda_y=4\pi^2\sigma/(k_xk_y)=8\pi^2\sigma/(k^2\sin 2\theta)\,, \tag{4·2}$$

where θ is defined in Eq. (4·1). Because the axis ratio of a filament, $a_y(t)/a_x(t)$, changes as the perturbation grows, it is a function of $\delta\rho/\rho_{00}$. When density becomes high enough and a cloud becomes opaque, the collapse will stop. The axis ratio of this opaque cloud is denoted as R_f which is a function of θ. Because it is most probable for a filament to fragment with a wave length $\sim 2\pi\times$radius, the number of fragments $N(\theta)$ is given by

$$N(\theta)=R_f(\theta)/2\pi\,. \tag{4·3}$$

If all the mass given by Eq. (4·2) of one mode accretes to $N(\theta)$ fragments, each fragment's mass will be

$$m(\theta)=M(\theta)/N(\theta)=16\pi^3\sigma/(k^2R_f(\theta)\sin 2\theta)\,. \tag{4·4}$$

Now we consider cases where the values of $\delta\rho/\rho_{00}$ at the time when the cloud becomes opaque are 10^2 and 10^3. And if we assume that the initial number of waves is independent of θ and use the value of R_f read from Fig. 12, we obtain from Eqs. (4·3) and (4·4) the mass function of fragments written in the form, $N=N(m)$, i.e., the number in the mass range $m-m+dm$ is $N(m)dm$. The results are shown in Fig. 14, where the number versus mass relation is obtained from the computational results for $k_y/k_x=1.2$, 1.5, 2.0 and 3.0. If we neglect the non-fragmentation case where $k_y/k_x\leqq 1.2$, the number N is nearly proportional to m^{-2}. This result is very suggestive to the explanation of observational data for pre-main sequence stars and dense clouds in Taurus region, where the mass function is nearly equal to m^{-2}.[9),10)]

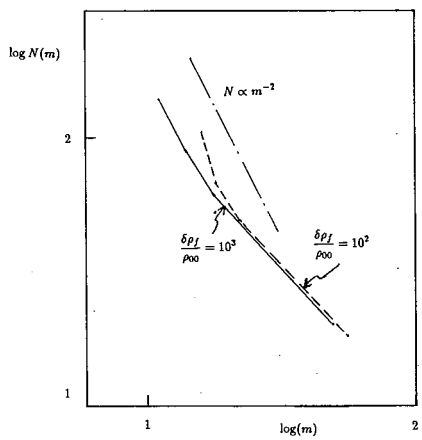

Fig. 14. The number versus mass relation for the final fragments of clouds. The value of $\delta\rho_f/\rho_{00}$ denotes the final value of $\delta\rho/\rho_{00}$ when the collapse stops.

4.3. *Conclusions*

A) We investigated the growth of perturbation of the mode, $\cos(k_xx)\cos(k_yy)$, existing initially in the isothermal sheet cloud by means of fully-nonlinear simulation. The results are as follows.

(1) The growth time of perturbation depends mainly on the wave number $k(=\sqrt{k_x^2+k_y^2})$.

(2) The shape of the density contours and its evolution depend strongly on the ratio

k_y/k_x.
(3) If $1/1.2 \leqq k_y/k_x \leqq 1.2$, the perturbation grows axisymmetrically and the density distribution in the $z=0$ plane is given by $\rho \propto R^{-2}$. The shape of the equi-density surface of the fragment is not spherical but sightly flattened. This flatness is not so large (~ 2) and hence this fragment will not break up again.
(4) If $k_y/k_x > 1.2$ or $< 1/1.2$, the perturbation grows to form a collapsing filament. The collapse is essentially equal to the isothermal cylindrical collapse. Namely, the cylinder collapses in the direction perpendicular to the cylindrical axis and the density distribution in the outer region is nearly given by R^{-4} (R being the radial distance from the axis).
B) If we assume that the initial spectrum of perturbations is independent of the ratio k_y/k_x, about 90% of the perturbations grow to form thin filaments. This has been confirmed by simulation for the case of random velocity fluctuations.
C) Finally we can construct a scenario of cloud's fragmentation. According to this scenario, the mass function of final fragments is almost proportional to m^{-2}.

Acknowledgements

The numerical computations were performed by FACOM VP-200 at the Data Processing Center of Kyoto University. This work was supported by the Grant-in-Aid for Scientific Research of the Ministry of Education, Science and Culture of Japan (No. 59740123, 61740140, 60300013 and 62460039).

Appendix

—— Method of Computing Gravitational Force ——

We consider how to solve numerically the Poisson equation

$$\partial^2 \Psi/\partial x^2 + \partial^2 \Psi/\partial y^2 + \partial^2 \Psi/\partial z^2 = 4\pi G\rho \,. \tag{A·1}$$

Because density obeys the periodic condition given by Eq. (2·3), we have

$$\rho(x \pm x_b, y \pm y_b) = \rho(x, y), \quad -x_b/2 < x \leqq x_b/2, \quad -y_b/2 < y \leqq y_b/2 \,. \tag{A·2}$$

We solve Eq. (A·1) in a rectangular box with the side lengths, x_b, y_b and $2.4z_b$. The side lengths of x_b and y_b are divided into N_x and N_y grids with equal intervals. In the z-direction, the region with $|z| \leqq 1.2z_b$ is divided into N_z grids. Let the value of density at the grid point (a, b) be denoted by $\rho_{a,b}(z)$. Then, because of the periodicity of the density and the potential, they can be expressed as the Fourier series

$$\rho_{a,b}(z) = \sum_{m=0}^{N_x-1} \sum_{n=0}^{N_y-1} \hat{\rho}_{m,n}(z) \exp(2\pi i(am/N_x + bn/N_y)) \,. \tag{A·3}$$

$$\Psi_{a,b}(z) = \sum_{m=0}^{N_x-1} \sum_{n=0}^{N_y-1} \hat{\Psi}_{m,n}(z) \exp(2\pi i(am/N_x + bn/N_y)) \,. \tag{A·4}$$

The operators $\partial^2/\partial x^2$ and $\partial^2/\partial y^2$ in Eq. (A·1) are changed into a finite difference operator, i.e.,

$$\partial^2/\partial x^2 \longrightarrow \Delta x^{-2} \cdot (\Psi(x+\Delta x) + \Psi(x-\Delta x) - 2\Psi(x)) \,, \tag{A·5}$$

where Δx is the grid interval. Then, $\hat{\Psi}_{m,n}(z)$ must satisfy

$$d^2/dz^2(\hat{\Psi}_{m,n}(z))-\kappa_{m,n}^2\hat{\Psi}_{m,n}(z)=4\pi G\hat{\rho}_{m,n}(z)\,, \tag{A·6}$$

where

$$\kappa_{m,n}^2=(4/\Delta x^2)\sin^2(\pi m\Delta x/N_x)+(4/\Delta y^2)\sin^2(\pi n\Delta y/N_y)\,. \tag{A·7}$$

We can obtain the Green function $G_{m,n}$ of Eq. (A·6) as

$$\left.\begin{aligned} &G_{m,n}(z,z')=(1/2\kappa_{m,n})\exp(-\kappa_{m,n}|z-z'|)\,, \quad \text{if } m\neq 0 \text{ or } n\neq 0\\ &G_{0,0}(z,z')=-(1/2)|z-z'|\,. \end{aligned}\right\} \tag{A·8}$$

If the density distribution in the z-direction is approximated as

$$\rho_{m,n}(z)=\sum_k \rho_{m,n}(z_k)\delta(z-z_k)\,, \tag{A·9}$$

then we can obtain at the grid point $z=z_i$,

$$\begin{aligned} \hat{\Psi}_{m,n}(z_i)&=-4\pi G\int \hat{\rho}_{m,n}(z')G_{m,n}(z_i,z')dz'\\ &=-4\pi G\sum_j \hat{\rho}_{m,n}(z_j)G_{m,n}(\Delta z(i-j))\,, \end{aligned} \tag{A·10}$$

where Δz is the grid size in the z-direction. Now $\Psi_{a,b}$ is obtained from Eq. (A·4). The Fourier transformation is carried out very quickly using FFT algorithm. Then we calculate the gravitational forces at the grid points and interpolate them to the value at the particle center.

References

1) S. M. Miyama, S. Narita and C. Hayashi Prog. Theor. Phys. **78** (1987), 1051. (Paper I)
2) S. M. Miyama, S. Narita and C. Hayashi, Astrophys. J. **279** (1984), 621.
3) S. M. Miyama, M. Sekiya, S. Narita and C. Hayashi, in preparation.
4) M. V. Penston, Mon. Not. R. Astron. Soc. **144** (1969), 425.
5) R. B. Larson, Mon. Not. R. Astron. Soc. **145** (1969), 271.
6) S. Narita, C. Hayashi and S. M. Miyama, Prog. Theor. Phys. **72** (1984), 1118.
7) M. Gaida, H. Ungerechts and G. Winnewisser, Astron. Astrophys. **137** (1984), 17.
8) R. B. Larson, Mon. Not. R. Astron. Soc. **214** (1985), 379.
9) M. Cohen and L. V. Kuhi, Astrophys. J. Suppl. **41** (1979), 743.
10) Y. Tomita, private communication (1986).